Size effects in microstructured superconductors and quantum materials

Fermin, R.

3

REDUCING DIMENSIONS: THE THIN FILM PLANAR JOSEPHSON JUNCTION

R. Fermin, B. de Wit & J. Aarts

The magnetic field dependent critical current $I_c(B)$ of a Josephson junction is determined by the screening currents in its electrodes. In macroscopic junctions, a local vector potential drives the currents, however, in thin film planar junctions, with electrodes of finite size and various shapes, they are governed by non-local electrodynamics. This complicates the extraction of parameters such as the geometry of the effective junction area, the effective junction length and, the critical current density distribution from the $I_c(B)$ interference patterns. In Phys. Rev. B, ***81****, 144515 (2010), John Clem derived $I_c(B)$ for Josephson junctions separating a rectangular superconducting strip of length L and width W. In this chapter, we will extend his technique to find $I_c(B)$ for junctions with ellipsoid and rhomboid geometries. We find the periodicity of the interference pattern ΔB to have common limits for $L \gg W$ and $L \ll W$, independent of the geometry. By fabricating elliptically shaped S−N−S junctions with various aspect ratios, we experimentally verify the L/W dependence of ΔB. We show that these results greatly affect the Fourier relation between $I_c(B)$ and the distribution of critical current in the junction, which makes incorporating these alterations essential for the correct analysis of current channels in topological and magnetic planar Josephson junctions.*

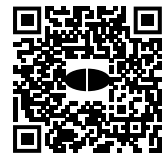

A paper based on this chapter is under review for publication in *Phys. Rev. B* and is published as preprint at arXiv.org under the identifier 2210.05388.

3.1. INTRODUCTION

The previous chapter deals with junctions that are orders of magnitude larger than the physical length scales governing their physics. The discussion of Josephson junctions and their associated interference patterns becomes radically different when the size of the superconducting electrodes is constricted in one or more dimensions. Specifically, when the junction is formed between two superconducting thin films, with a thickness below λ_L, the shielding current running along the junction, responsible for the shape and periodicity of the magnetic interference in the critical current $I_c(B)$, is no longer determined by the Meissner effect in its macroscopic form (i.e., by the local vector potential). Rather non-local electrodynamic effects start to play a role[1–4]. This can be understood by considering that the magnitude of the shielding currents remains the same when the thickness of the superconducting electrode is decreased (there are no sample dimensions in Eq. 2.11). Therefore, the current density in the electrodes increases, and it becomes energetically favorable to extend the shielding currents deeper into the electrodes, yielding a larger penetration depth or effective junction length. In numerous theoretical and experimental studies, it was found that in thin film planar junctions, $I_c(B)$ becomes completely independent of λ_L and is solely determined by the geometry of the sample[4–8]. Moreover, John Clem provided a method to calculate $I_c(B)$ for planar junctions that are also restricted in their lateral size, i.e., a Josephson junction separating a rectangular superconducting strip of width W and length L in two halves[7].

In light of the disk- and ellipse-shaped thin film planar S−F−S junctions presented in Part two, we will review his technique in this chapter and extend his work by covering two more geometries: the ellipse and the rhomboid, both of width W and length L. First, we calculate $I_c(B)$ for these geometries and extract the periodicity of the interference pattern ΔB for different ratios of L/W. Next, we experimentally verify the geometry dependence of ΔB by fabricating elliptically shaped S−N−S junctions with different ratios of L/W. Finally, we analyze how the Fourier relation between $I_c(B)$ and the critical current density distribution is altered for these planar junctions. We find that adapting the Fourier transform is crucial in predicting the location of possible current channels in thin film planar junctions.

3.2. REVIEW OF THE CLEM MODEL

As we examine the thin film limit, the screening current density is uniform in the film, which effectively reduces the problem to a semi-2D one. Therefore, we consider a normal metal Josephson junction (dimensions W and d) that divides a symmetric superconducting thin film into two halves. We specifically consider the junction to be in the short junction limit, as the original model by Clem treats an infinitesimally thin insulating tunnel junction. Furthermore, it is assumed that the electrode the electrode

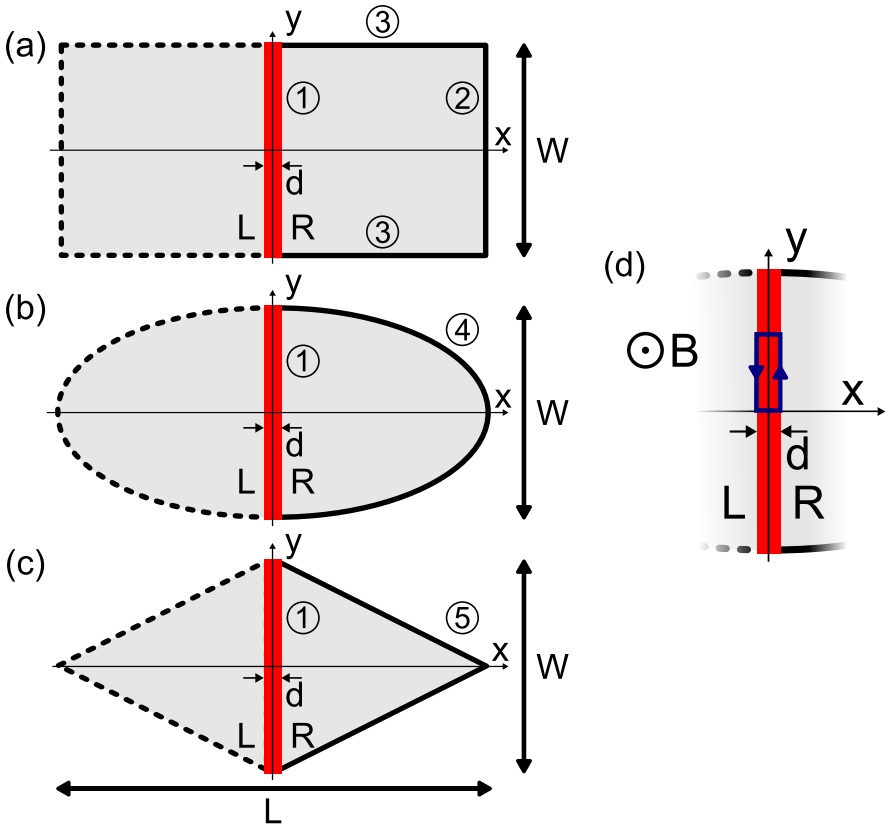

Figure 3.1: Schematics of the three geometries used for calculations in this chapter, being (a) the rectangle, (b) the ellipse and (c) the rhombus. They resemble superconducting thin films of width W and length L, which are separated by a normal metal junction of width d (colored red). By numbers we indicate different sections of the right electrode edge. The boundary conditions for these are summarized in Table 3.1. In (d) we show a zoom of the junction area under the magnetic induction $\boldsymbol{B} = B\hat{z}$. The dark blue path is used as loop integral to determine $I_c(B)$.

dimensions are smaller than the Pearl length, given by:

$$\Lambda = \frac{2\lambda_L^2}{t_{\text{film}}} \tag{3.1}$$

Here t_{film} the thickness of the superconducting films. This implies that the self fields of the screening currents are far smaller than the applied external field. Additionally we assume that the junction is in the narrow limit, meaning that the junction is less wide than the Josephson penetration length, which for planar junctions in the thin film limit is the given by[4, 5, 7]:

$$l = \frac{\Phi_0 t_{\text{junc}} W}{4\pi\mu_0 \lambda_{\text{L}}^2 I_{\text{c}}(0)} \tag{3.2}$$

Here t_{junc} is the thickness of the junction. Figure 3.1 shows a schematic of three of such films, having different geometries. The junction, colored red in Figure 3.1, is running along the y-direction from $-W/2$ to $W/2$. In Figure 3.1d, we sketch a zoom of a junction, where we specify the integration contour (similar to Figure 2.3) under a magnetic induction of $\boldsymbol{B} = B\hat{z}$. In order to calculate $I_{\text{c}}(B)$, the current running along this integration contour $J_y(\frac{d}{2}, y)$ needs to be evaluated. To do so, first note that the supercurrent is conserved and therefore $\boldsymbol{\nabla} \cdot \boldsymbol{J} = 0$. By choosing the convenient gauge $\boldsymbol{A} = -yB\hat{x}$, we find $\nabla \times \boldsymbol{A} = B\hat{z} = \boldsymbol{B}$ and $\nabla \cdot \boldsymbol{A} = 0$. Therefore, the divergence of the second Ginzburg-Landau equation (Eq. 2.4) reduces to:

$$\nabla^2 \gamma = 0 \tag{3.3}$$

Here γ is the gauge-covariant phase of the superconducting wave function, and we recognize that we mapped the second Ginzburg-Landau equation onto the Laplace equation. With sufficient boundary conditions, it can be solved for a unique solution, which allows us to calculate $J_y(\frac{d}{2}, y)$. The boundary conditions arise from the prerequisite that no supercurrent can exit the sample at its outer boundaries. Furthermore, we assume a weak Josephson coupling, meaning that the shielding currents in the electrodes are far larger than the Josephson currents between the electrodes, which we approximate as $J_x(\frac{d}{2}, y) = 0$. Therefore we can write:

$$\boldsymbol{J} \cdot \hat{\boldsymbol{n}}_{\text{R}} = 0 \tag{3.4}$$

Where $\hat{\boldsymbol{n}}_{\text{R}}$ is the unit vector, normal to the outer edges of the right electrode. Combined with the second Ginzburg-Landau equation, this leads to a set of Neumann boundary conditions:

$$(\boldsymbol{\nabla}\gamma) \cdot \hat{\boldsymbol{n}}_{\text{R}} = -\frac{2\pi}{\Phi_0} \boldsymbol{A} \cdot \hat{\boldsymbol{n}}_{\text{R}} \tag{3.5}$$

Which is sufficient to solve for $\gamma(x, y)$. Next, Eq. 2.28 allows us to find the gauge-invariant phase difference over the junction $\varphi(y)$. Note that we have conveniently chosen $A_{\text{y}} = 0$. We then find:

$$2\mu_0\lambda_L^2\int_0^y J_{y,R}\left(\frac{d}{2},y'\right)\mathrm{d}y' = 2\int_0^y \frac{\mathrm{d}\gamma}{\mathrm{d}y'}\left(\frac{d}{2},y'\right)\mathrm{d}y' = 2\gamma\left(\frac{d}{2},y\right) \tag{3.6}$$

Therefore, $\varphi(y)$ is given by the simple expression:

$$\varphi(y) = \varphi(0) + \frac{2\pi dB}{\Phi_0}y + 2\gamma\left(\frac{d}{2},y\right) \tag{3.7}$$

Finally, $I_c(B)$ is found by following the discussion in Chapter 2:

$$\frac{I_c(B)}{I_c(0)} = \frac{1}{W}\left|\int_{-W/2}^{W/2}\cos\left(\frac{2\pi dB}{\Phi_0}y + 2\gamma\left(\frac{d}{2},y\right)\right)\mathrm{d}y\right| \tag{3.8}$$

We see that finding $I_c(B)$ becomes equal to a boundary condition problem of solving the Laplace equation in the geometry of the electrodes. Indeed, the solution is completely determined by the geometry of the sample and is independent of λ_L.

3.3. COMPARING DIFFERENT GEOMETRIES

As it is not trivial to find a general analytical solution to the boundary problem of Eq. 3.3 for the ellipsoid and rhomboid geometries, we solve the Laplace equation numerically using COMSOL Multiphysics 5.4. We define the right electrode geometry in 2D, divided into a triangular grid, on which COMSOL carries out the calculations. Crucial for correctly solving Eq. 3.3, is a grid size that is small enough to capture small changes

Boundary	$(\nabla\gamma)\cdot\hat{\boldsymbol{n}}_\Omega$
①	$\frac{2\pi B}{\Phi_0}y$
②	$-\frac{2\pi B}{\Phi_0}y$
③	0
④	$\frac{2\pi B}{\Phi_0}\frac{Wxy}{L\sqrt{(\frac{Wx}{L})^2+(\frac{Ly}{W})^2}}$
⑤	$-\frac{2\pi B}{\Phi_0}\frac{Wy}{\sqrt{W^2+L^2}}$

Table 3.1: The Neumann boundary conditions for each edge section, listed by the numbering used in Figure 3.1.

in γ and, on the edges, $\hat{\boldsymbol{n}}_{\mathrm{R}}$. We found a maximum element size (i.e., the grid edge size) of $0.01\ln(1+L/W)$ nanometer to be a good compromise between computation time and precision. Using trigonometry we evaluate $\boldsymbol{A}\cdot\hat{\boldsymbol{n}}_{\mathrm{R}}$ for each geometry and list the corresponding boundary conditions in Table 3.1 (here the numbering corresponds to the numbers in Figure 3.1).

3.3.1. SIMULATION RESULTS

Clem showed that the analytical solution for the rectangular geometry is an infinite series of sines and hyperbolic tangents. For the rectangle, this leads to the maximum in $\gamma\left(\frac{d}{2},y\right)$ to occur at $W/2$, which can be approximated as:

$$\gamma\left(\frac{d}{2},\frac{W}{2}\right)=\frac{7\,\zeta(3)}{\pi^2}\frac{BW^2}{\Phi_0}\tanh\left(\frac{\pi^3}{28\,\zeta(3)}\frac{L}{W}\right) \tag{3.9}$$

Here ζ is the Riemann zeta function. Now we generalize this approximation to include the other geometries. We find that the simulated $\gamma\left(\frac{d}{2},y\right)$ universally follows:

$$\gamma\left(\frac{d}{2},y\right)=\frac{7\,\zeta(3)}{\pi^2}\frac{BW^2}{\Phi_0}\tanh\left(\frac{\pi^3}{28\,\zeta(3)}\frac{A}{W^2}\right)f\left(\frac{y}{W}\right) \tag{3.10}$$

Where $f\left(\frac{y}{W}\right)$ is a dimensionless function defined by the specific geometry and A is the total surface area of the electrodes. Note that we have substituted $\frac{L}{W}$ in the argument of the hyperbolic tangent for $\frac{A}{W^2}$; the reason for this choice will become apparent below when discussing the period of the $I_{\mathrm{c}}(B)$-pattern. Figure 3.2a shows the calculated $\gamma(x,y)$ for a disk geometry (i.e., an ellipse where $L=W$), normalized to the applied magnetic field and width of the junction $\gamma\Phi_0/BW^2$. We plot $f\left(\frac{y}{W}\right)$ for this disk in Figure 3.2b. Since $\gamma(y)$ (and therefore $\varphi(y)$ as well) scale linearly with the magnetic field, we can evaluate the integral of Eq. 3.8 numerically for different values of B. The resulting interference pattern (Figure 3.2c) resembles a Fraunhofer pattern at first sight. However, the peak height decreases less strongly than $1/B$, and the width of the middle lobe is not twice the width of the side lobes. In the inset of Figure 3.2c, we plot the width of the nth side lobe (ΔB_{n}); the width increases and reaches an asymptotic value for large n.

In order to compare the interference patterns of junctions of different geometry, we define the period of the oscillations to be the width of the fifth side lobe ($\Delta B=\Delta B_5$). In the inset of Figure 3.2c, this is shown by the vertical reference line. The width of the fifth side lobe is not only sufficiently close to the asymptotic value but also experimentally accessible without the need for large magnetic fields. We now compare the periodicity of the interference patterns for different geometries by plotting the dimensionless

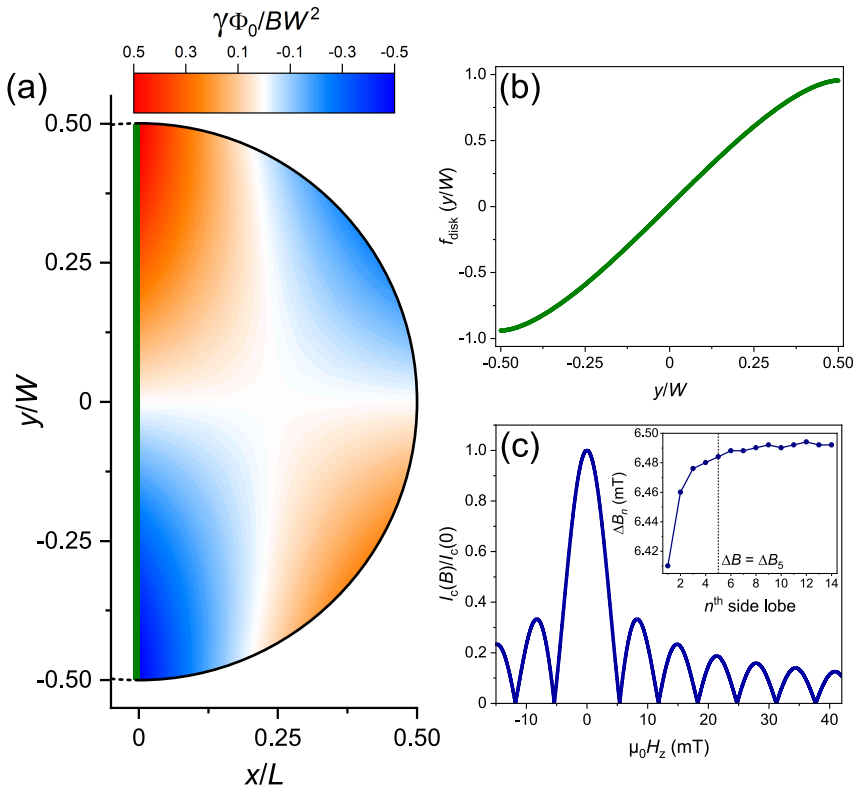

Figure 3.2: (a) Gauge-covariant phase simulated in the right electrode of a disk-shaped planar Josephson junction, normalized to the applied magnetic field and width of the junction $\gamma\Phi_0/BW^2$. The junction is shown as a green line. This result lets us extract the gauge-covariant phase along the junction. It follows the scaling of Eq. 3.10, and it is determined by a dimensionless function, which is plotted in (b). (c) Shows the interference pattern calculated integration of the result in (a) using Equation 3.8 for different values of B. The typical interference pattern looks like a Fraunhofer pattern at first sight. However, the peak height decreases less strongly than $1/B$, and the width of the side lobes is larger than half of the middle lobe, which is 10.76 mT wide. Furthermore, the width of the nth side lobe increases and reaches an asymptotic value for large values of n, which is evident from the inset of (c), where we plot the width of the nth side lobe. The width of the fifth side lobe is used for comparisons between simulations and experiments.

value $\Delta BW^2/\Phi_0$ as a function of the aspect ratio L/W in Figure 3.3a on a log-log scale. First, we find the results obtained on the rectangular junction to match the analytical results obtained by Clem[7]. Furthermore, the periodicity of the pattern increases as the sample dimensions are diminished. In a laterally smaller sample, the screening currents are more confined to the junction, and therefore the effective length L_{eff} is smaller, yielding a larger ΔB. Finally, we evaluated the width of the junction (d) to be irrelevant in determining ΔB. Specifically, its contribution to the period is in the μT range for realistic sizes of d. The consequence is that ΔB is determined by the maximum of γ, i.e., $\gamma(\frac{d}{2}, \frac{W}{2})$.

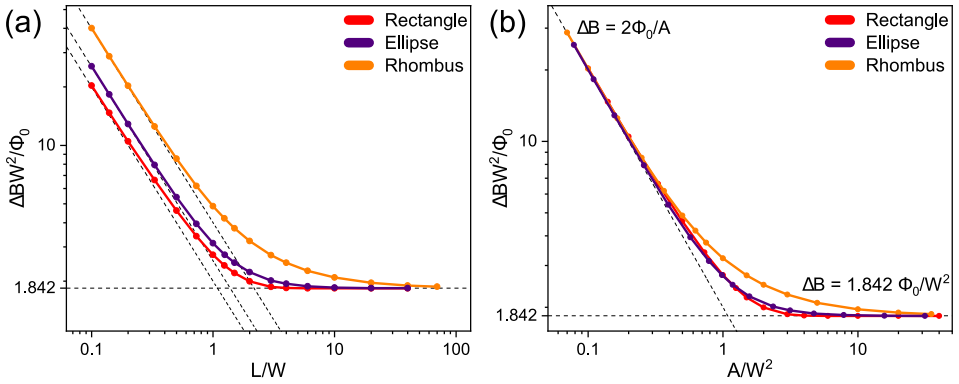

Figure 3.3: dimensionless measure of the period ΔB (the width of the fifth side lobe) of the calculated interference pattern $I_c(B)$ for the three geometries. In (a) we plot this value on log-log scale versus the aspect ratio L/W, in (b) it is plotted versus the total electrode area A, scaled by the width of the film squared. Figure (b) reveals two limits for ΔB for $L \gg W$ and $L \ll W$. The first corresponds to the limit of an infinite superconducting strip $\Delta B = 1.842\Phi_0/W^2$, whereas in the latter we find $\Delta B = 2\Phi_0/A$. Contrary to ΔB, $I_c(B)$ itself is not geometry independent in this limit.

ΔB reaches asymptotic values for the limits $L \gg W$ and $L \ll W$ for all three geometries. The value of ΔB becomes geometry independent in these limits, as revealed by rescaling the results from Figure 3.3a to a $\frac{A}{W^2}$ dependence, displayed in Figure 3.3b. In the first limit, $L \gg W$, all three geometries become an infinite superconducting strip. Here we find $\Delta B = 1.842\Phi_0/W^2$, which matches literature[6, 7]. In this limit, we find $\gamma\left(\frac{d}{2}, y\right)$ to follow:

$$\gamma\left(\frac{d}{2}, y\right) = \frac{7\,\zeta(3)}{\pi^2}\frac{BW^2}{\Phi_0} f_{\text{strip}}\left(\frac{y}{W}\right) = \frac{\pi}{2}\frac{1}{1.842}\frac{BW^2}{\Phi_0} f_{\text{strip}}\left(\frac{y}{W}\right) \tag{3.11}$$

Where $f_{\text{strip}}\left(\frac{y}{W}\right)$ is a dimensionless function running from -1 to 1, plotted in Figure 3.4a. In the other limit, $L \ll W$, Eq. 3.10 reduces to:

$$\gamma\left(\frac{d}{2}, y\right) = \frac{\pi AB}{4\Phi_0} f\left(\frac{y}{W}\right) = \frac{\pi}{2}\frac{AB}{2\Phi_0} f\left(\frac{y}{W}\right) \tag{3.12}$$

Figure 3.4b shows $f\left(\frac{y}{W}\right)$ in the limit $L \ll W$, for all three geometries. Since the maximum of $f\left(\frac{y}{W}\right)$ becomes independent of the underlying geometry and equal to unity, we find a geometry independent period, where $\Delta B = 2\Phi_0/A$. We can generalize this concept to find a general expression for ΔB:

$$\Delta B = \frac{\pi}{2}\frac{1}{\max(\gamma/B)} = \frac{\pi}{2}\frac{B}{\gamma(\frac{d}{2}, \frac{W}{2})} \tag{3.13}$$

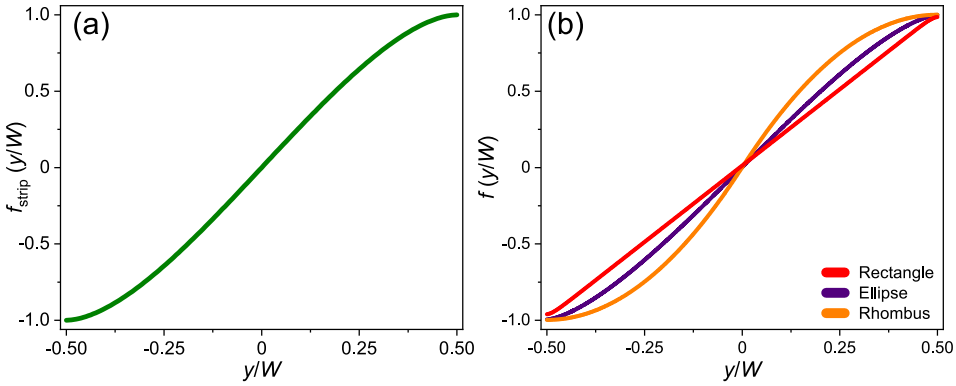

Figure 3.4: dimensionless scaling functions $f\left(\frac{y}{W}\right)$ from Eq. 3.10, for the limit $L \gg W$ in (a) and $L \ll W$ in (b). The maximum of these functions is located at $y = |W/2|$ and equals unity. Therefore, ΔB (large n limit of the nth side lobe of $I_c(B)$) is universal for these limits. However, for the limit $L \ll W$, $f\left(\frac{y}{W}\right)$ is not geometry independent, which means $I_c(B)$ itself is not geometry independent in this limit.

Note that $\max(f\left(\frac{y}{W}\right)) \approx 1$ for all ratios L/W, and thus Eq. 3.13 can serve as a good approximation for ΔB. Therefore, we justify the relation of Eq. 3.10 as it demonstrates the emerging universal limits where $\Delta B = 2\Phi_0/A$ and $\Delta B = 1.842\Phi_0/W^2$, as well as provides a good approximation of ΔB between the limiting cases.

Although ΔB is geometry independent in the limit $L \ll W$, $I_c(B)$ itself is not universal in this limit. This is caused by the fact that $f\left(\frac{y}{W}\right)$ differs between geometries for $y \neq |W/2|$. For the rectangular geometry, for example, this function is linear in y: $f\left(\frac{y}{W}\right) = \frac{2y}{W}$. Therefore, we retrieve the Fraunhofer pattern, where $L_{\text{eff}} = L/2 + d$. The effective length equals the length of a single superconducting electrode plus the junction length. This can be understood by considering that the screening currents trace loops in the electrodes, that reduce to two parallel and opposite current tracks, when $L \ll W$. The tracks that contribute to $J_y(\frac{d}{2}, y)$ effectively cover half of each electrode, yielding $L_{\text{eff}} = L/4 + L/4 + d$. $\gamma\left(\frac{d}{2}, y\right)$ in the rhomboid geometry is radically different; it is well approximated by a sine function: $f\left(\frac{y}{W}\right) = \sin\left(\frac{\pi y}{W}\right)$. This leads to an interference pattern that is far closer to the pattern shown in Figure 3.2c, and not a Fraunhofer pattern. In conclusion: the shape and periodicity of the $I_c(B)$-pattern for low magnetic fields is independent of ΔB_n in the limit of large n, which is universal for $L \ll W$.

3.3.2. COMPARISON TO EXPERIMENTS

In order to verify the dependence on the geometry, we have fabricated five ellipse-shaped planar S−N−S junctions for different ratios of L/W. Besides, we made a rectangular-shaped junction with dimensions well in the $L \gg W$ limit.

First, a four-probe contact geometry is patterned on Si substrates using electron-beam lithography. Next, an Ag (20 nm), MoGe (55 nm) bilayer is deposited by sputter deposition. Next, we use Focused Ion beam (FIB) milling to structure elliptical devices in the bilayer. By applying an ultra-low beam current of 1.5 pA, the weak link is formed by a line cut in the MoGe layer at the center of the device. This completely removes the superconductor on top but leaves a normal metal connection. The resulting trench

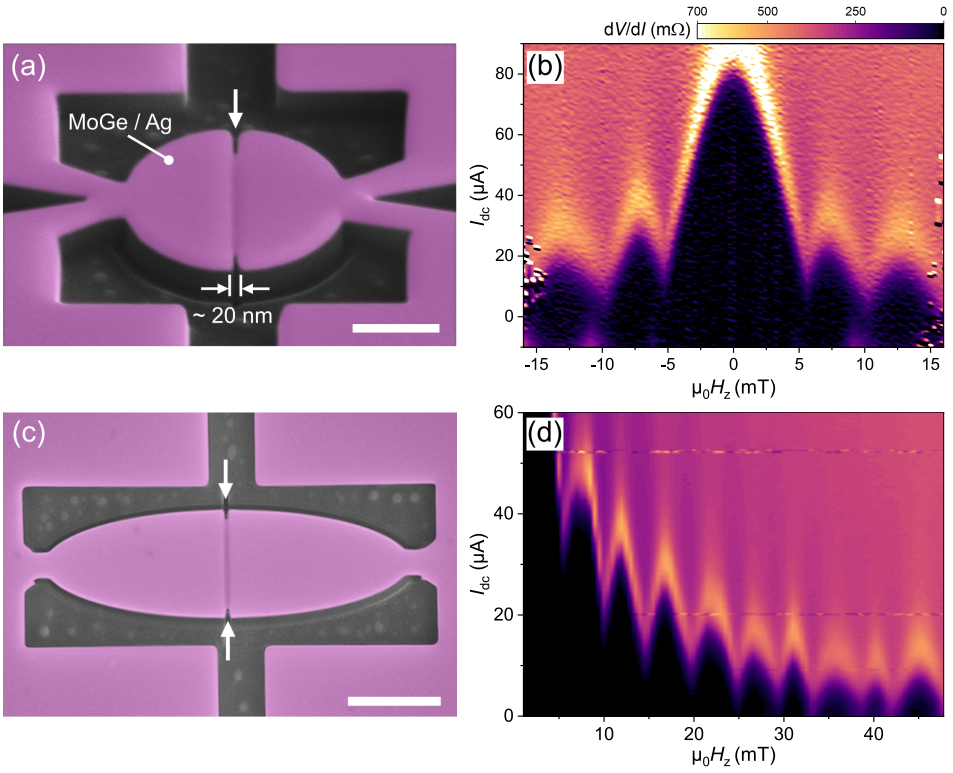

Figure 3.5: Two S−N−S junction samples with a circular and ellipsoid geometry, produced from an Ag/MoGe bilayer and their corresponding $I_c(B)$-patterns. (a) A false colored scanning electron micrograph of a disk-shaped sample, viewed under an angle. The white arrow indicates the junction. Note the notches on the side of the sample due to an increased milling rate at the edges of the disk. The scale bar equals 500 nm. The corresponding $I_c(B)$, displayed in (b), is a Fraunhofer-like pattern. As expected, the peak height of the side lobes is decreasing less rapidly than $1/B$. Contrary to the calculated pattern in Figure 3.2c, the middle peak is twice as wide as the neighboring ones. (c) depicts a top-view false colored scanning electron micrograph of an ellipse-shaped junction. Again we indicate the notches with white arrows; the scale bar represents 1 μm. In (d), we plot the corresponding interference pattern, which is used to extract the periodicity of the oscillations.

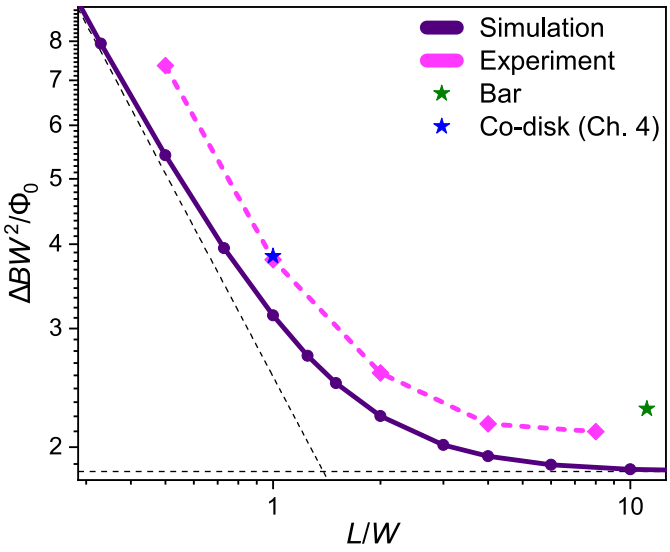

Figure 3.6: Calculated periodicity ΔB of the fifth lobe of the interference pattern $I_c(B)$ obtained for the ellipse-shaped samples, compared to experimentally acquired values. We plot the dimensionless measure $\frac{\Delta BW^2}{\Phi_0}$ versus the aspect ratio L/W. The blue star indicates the periodicity of the cobalt disk junctions discussed in Chapter 4 and the green star represents the results obtained on a bar shaped sample. Although we can well predicted the L/W-dependence, we find a constant offset between the experimental values and the simulations. This can be explained by the notches visible in Figure 3.5a and 3.5c, which make the junction width shorter than the width of the electrodes (W).

separates the MoGe electrodes by a roughly 20 nm weak link, allowing Josephson coupling in this S−N−S system. Figures 3.5a and 3.5c show false colored scanning electron micrographs of two of such devices, for $L = W$ and $L = 4W$ respectively. We follow the same fabrication procedure for the S−F−S devices presented in Chapters 4 and 5.

Two corresponding interference patterns obtained on the samples in 3.5a and 3.5c are shown in Figure 3.5b and 3.5d. Clearly, the period of the interference patterns scales with L/W. However, we find that the middle peak is twice the width of the neighboring ones and the amplitude of the side lobes of the $I_c(B)$-pattern feature a similar width, instead of the asymptotic behavior predicted by our theory (see Figure 3.2c). This can be explained by the fact that $l \approx 100$ nm (Eq. 3.2; based on $\lambda = 535$ nm[9]), which is small with respect to W. Our samples are therefore not in the narrow junction limit and allow Josephson vortices to stabilize in the junction. The width of the middle lobe can therefore not be predicted by our theory. However, Boris et al. have shown that ΔB_n for large n still follows the predictions of non-local electrodynamics[4]. Therefore, we can still compare the measured ΔB to our theoretical model.

To compare the period of the $I_c(B)$-pattern to our theory, we extract the width of the fifth lobe of the interference pattern for all measured samples and plot it along with the calculated values in Figure 3.6a. By star symbols, we also mark the periodicity of the os-

cillations of the Co-based S−F−S junctions discussed in Chapter 4 and the periodicity of the bar-shaped sample. Although there is a constant offset between the measured periodicity and the calculated values, the overall trend is well predicted.

This constant offset can be explained by a trivial side effect of the FIB structuring method. During FIB processing, removed material is redeposited elsewhere on the sample. Even though redeposition does not affect the devices, it leads to a dependence of the milling rate on the geometry. A more exposed part of the sample, i.e., the edges of the device, will mill faster than in the bulk of the material. Consequently, notches develop on the side of the device when milling the trench. These notches make the width of the weak link slightly smaller than the width of the electrodes, which can result in a constant offset between the simulations and experiments. A method of accounting for the influence of the notches is modifying the Fourier transform for application to thin film planar junctions, which I will discuss below.

However, there is also an inconsistency between our experimental data and the theory. We cannot explain why the rectangular-shaped junction exhibits an $\Delta BW^2/\Phi_0$ that is larger than our ellipses with high L/W-ratios. In fact, in the limit of $L \gg W$, we expect a universal limit that is independent of the size of the notches (see for example references [10] and [11]). At the moment this is unexplained.

3.4. CONSEQUENCES FOR THE FOURIER ANALYSIS

In Chapter 2 it became clear that $I_c(B)$ is related to the critical current distribution in the junction, by Fourier transform. For macroscopic junctions, where the screening currents are Meissner-like, we have evaluated $\varphi_B(y) = \frac{2\pi L_{\text{eff}} B}{\Phi_0} y$. For the mesoscopic devices discussed here, this quantity needs to be replaced by Eq. 3.7, yielding:

$$I_c(B) = \left| \int_{-\infty}^{\infty} J_c(y) e^{i2\gamma\left(\frac{d}{2}, y\right)} \mathrm{d}y \right| = \left| \int_{-\infty}^{\infty} J_c(y) e^{i2\pi\left(\frac{7\,\zeta(3)}{\pi^3} \frac{BW^2}{\Phi_0} \tanh\left(\frac{\pi^4}{112\,\zeta(3)}\right) f_{\text{disk}}\left(\frac{y}{W}\right)\right)} \mathrm{d}y \right| \quad (3.14)$$

Where we omitted the contribution from the weak link, as its magnitude is negligible. In the second part we specified $\gamma\left(\frac{d}{2}, y\right)$ for a disk-shaped junction. Now we can define a new pair of conjugate variables: the length $\tilde{y} = W f_{\text{disk}}\left(\frac{y}{W}\right)$ and the reduced field $\tilde{\beta} = \frac{7\,\zeta(3)}{\pi^3} \frac{BW}{\Phi_0} \tanh\left(\frac{\pi^4}{112\,\zeta(3)}\right)$, to arrive at:

$$I_c(\tilde{\beta}) = \left| \int_{-\infty}^{\infty} \tilde{J}_c(\tilde{y}) e^{i2\pi\tilde{\beta}\tilde{y}} \mathrm{d}\tilde{y} \right| = |\mathfrak{I}_c| \quad (3.15)$$

Where we made a change of coordinates and $\tilde{J}_c$ is defined as:

$$\tilde{J}_c\left(\frac{\tilde{y}}{W}\right) = \frac{dg}{d\tilde{y}}\left(\frac{\tilde{y}}{W}\right) J_c\left(W g\left(\frac{\tilde{y}}{W}\right)\right) \tag{3.16}$$

Here the function $g\left(\frac{\tilde{y}}{W}\right)$ is the inverse of $f\left(\frac{y}{W}\right)$, or $g\left(\frac{\tilde{y}}{W}\right) = f^{-1}\left(\frac{y}{W}\right)$, dropping the subscript, as a similar procedure can be done for the general scaling relation of Eq. 3.10. We conclude that the Fourier transform is still valid, albeit including a rescaling of the axes to retrieve the actual current density distribution $J_c(y)$. In the next section I will detail how the Fourier analysis is carried out technically for a disk-shaped junction.

3.4.1. TECHNICAL DETAILS OF THE FOURIER ANALYSIS

The transform $\mathfrak{I}_c$ is complex and therefore its real and imaginary parts encode for the even and odd components in $I_c(\beta)$ respectively. Since the interference patterns discussed in this thesis are relatively symmetric (i.e., an even function of the applied magnetic field), we can assume $\mathfrak{I}_c$ to be dominantly real:

$$I_{c,\mathrm{even}}(\tilde{\beta}) = \int_{-\infty}^{\infty} \tilde{J}_{c,\mathrm{even}}(\tilde{y}) \cos(\tilde{\beta}\tilde{y})\, d\tilde{y} \tag{3.17}$$

Therefore the real part of $\mathfrak{I}_c$ is an oscillating function that flips sign at each zero crossing. The imaginary part is expected to be significantly smaller than the real part, except at the zero-crossing where the even part vanishes. Therefore, the imaginary part of $\mathfrak{I}_c$ ($I_{c,\mathrm{odd}}(\tilde{\beta})$) can be approximated by the critical current at the minima in the experimental interference pattern. Also $I_{c,\mathrm{odd}}(\tilde{\beta})$ is flipping its sign between each minimum and between the minima we approximate $I_{c,\mathrm{odd}}(\tilde{\beta})$ by linear interpolation. The inverse transform yielding $\tilde{J}_c(\tilde{y})$ from $I_c(\tilde{\beta})$ is then given by:

$$\tilde{J}_c(\tilde{y}) = \left| \int_{-\infty}^{\infty} \left(I_{c,\mathrm{even}}(\tilde{\beta}) + i\, I_{c,\mathrm{odd}}(\tilde{\beta})\right) e^{-i\tilde{\beta}\tilde{y}}\, d\tilde{\beta} \right| = \left| \int_{-\infty}^{\infty} \mathfrak{I}_c\, e^{-i\tilde{\beta}\tilde{y}}\, d\tilde{\beta} \right| \tag{3.18}$$

As discussed in the previous chapter, we find I_c from the data by a defining a voltage threshold; this is depicted in Figure 3.7a for a disk-shaped junction. We vertically translate the extracted I_c values such that the global minimum equals zero current. This step in the data analysis prevents the overestimation of $I_{c,\mathrm{odd}}(\tilde{\beta})$, which would result in an overly anti-symmetric current density distribution. $I_{c,\mathrm{even}}(\tilde{\beta})$ is found by multiplying the translated I_c by a flipping function that changes the sign of each subsequent lobe of the interference pattern, as can be observed in Figure 3.7b.

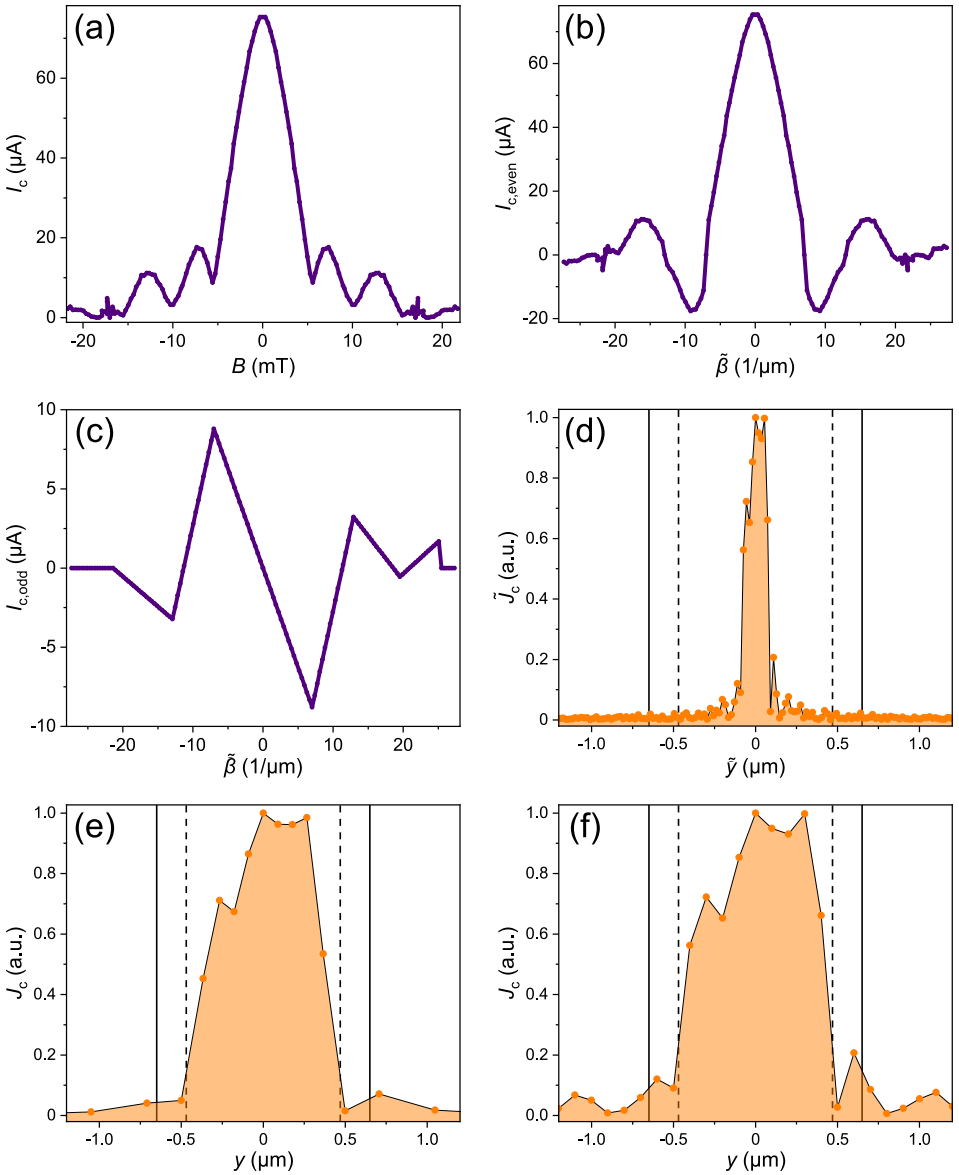

Figure 3.7: Overview of the subsequent steps of the Fourier transform analysis. (a) Extracted critical current on the basis of a voltage cut-off. In order to not overestimate the imaginary part of the complex critical current, the global minimum of the interference pattern is shifted to zero current. (b) and (c) respectively show the real and imaginary part of the complex critical current extracted from the interference pattern depicted in (a). Here the subsequent lobes are flipped to obtain the real part, and the minima are interpolated to obtain the imaginary part. (d) The resulting critical current density distribution, calculated using the Fourier transform described in Eq. 3.18. The result of (d) is scaled using $f_{\text{disk}}\left(\frac{y}{W}\right)$, to retrieve the actual $J_c(y)$, which is plotted in (e). Finally, in (f), we carried out a regular Fourier analysis using a linear approximation of $f_{\text{disk}}\left(\frac{y}{W}\right)$, circumventing the need for rescaling the axes. In (d), (e), and (f), we indicate the boundaries of the electrodes ($-W/2$ and $W/2$) by solid reference lines and the boundaries of the actual weak link (W minus the notches) by dotted reference lines. We find a uniform current density distribution, as expected for a single junction. The influence of the notches can be seen since no current flows outside the actual width of the weak link.

Here we also rescale the field axis to $\tilde{\beta}$. We follow the above procedure for finding $I_{c,odd}(\tilde{\beta})$, which is depicted in Figure 3.7c. The corresponding critical current density distribution is found by a numerical Fourier transform carried out in Python using the Numpy package, yielding the distribution $\tilde{J}_c(\tilde{y})$, depicted in Figure 3.7d. Finally both axes are rescaled using $f_{disk}\left(\frac{y}{W}\right)$ to retrieve $J_c(y)$, which is shown in Figure 3.7e.[1] Here we indicate $-W/2$ and $W/2$ by solid reference lines and the boundaries of the actual weak link by dotted reference lines. We observe a constant distribution of critical current throughout the junction, which is expected for a uniform S−N−S junction. Furthermore, the current is confined to the actual junction, not the full width of the superconducting film. This explains the constant offset in Figure 3.6a.

Note that the spatial resolution of current density distribution is determined by the field range in the measured $I_c(B)$-pattern, which is limited by the possible discontinuities, typically found in junctions with a ferromagnetic weak link. This sets a bound to the precision in determining the width of possible current channels. Furthermore, due to rescaling $\tilde{J}_c(\tilde{y})$ to $J_c(y)$, the binning becomes non-uniform, yielding a lower resolution near the edges of the device. As alternative, we carry out the Fourier transform using a linear approximation of $f_{disk}\left(\frac{y}{W}\right)$, depicted in Figure 3.7f. This mitigates the need for rescaling the axes and improves point density on the position-axis. Obviously, the linear approximation of $f_{disk}\left(\frac{y}{W}\right)$ breaks down near the edges, yielding less precise results.

3.5. CONCLUSION

In conclusion, this chapter analyzed the periodicity ΔB of the interference pattern $I_c(B)$ for thin film planar S−N−S Josephson junctions, both theoretically and experimentally. Specifically, we examine junctions separating rectangular, ellipsoid, and rhomboid films of width W and length L. By mapping the second Ginzburg-Landau equation to the two-dimensional Laplace equation, we solve $I_c(B)$ for different ratios of L/W. We show that ΔB has two universal limits for $L \gg W$ and $L \ll W$, independent of the sample geometry. The first corresponds to an infinite superconducting strip, and the latter is caused by an emerging universal dependence of the phase difference on the junction electrode surface area. By fabricating elliptically-shaped S−N−S junctions, having different ratios for L/W, we experimentally verify the geometry dependence of ΔB. Lastly, we adapt the Fourier relation between $I_c(B)$ and the critical current density distribution to suit planar junctions in the thin film limit. This proves to be vital in correctly predicting the location of current channels in the disk- and elliptically-shaped S−F−S junctions discussed in the next part of this thesis.

[1] For illustrative purposes, I have chosen to absorb part of the prefactor in $\tilde{y}$, as this this yields a larger contrast between Figure 3.7d and Figure 3.7e. Naturally, any choice of $\tilde{y}$ and $\tilde{\beta}$ is allowed, as long as it is consistent with γ.

REFERENCES

[1] Pearl, J. Current distribution in superconducting films carrying quantized fluxoids. *Appl. Phys. Lett.* **5**, 65–66 (1964).

[2] Ivanchenko, Y. & Soboleva, T. Nonlocal interaction in Josephson junctions. *Phys. Lett. A* **147**, 65–69 (1990).

[3] Abdumalikov, A. A., Jr., Alfimov, G. L. & Malishevskii, A. S. Nonlocal electrodynamics of Josephson vortices in superconducting circuits. *Supercond. Sci. Technol.* **22**, 023001 (2009).

[4] Boris, A. A. *et al.* Evidence for nonlocal electrodynamics in planar Josephson junctions. *Phys. Rev. Lett.* **111**, 117002 (2013).

[5] Kogan, V. G., Dobrovitski, V. V., Clem, J. R., Mawatari, Y. & Mints, R. G. Josephson junction in a thin film. *Phys. Rev. B* **63**, 144501 (2001).

[6] Moshe, M., Kogan, V. G. & Mints, R. G. Edge-type Josephson junctions in narrow thin-film strips. *Phys. Rev. B* **78**, 020510(R) (2008).

[7] Clem, J. R. Josephson junctions in thin and narrow rectangular superconducting strips. *Phys. Rev. B* **81**, 144515 (2010).

[8] Rodan-Legrain, D. *et al.* Highly tunable junctions and non-local Josephson effect in magic-angle graphene tunnelling devices. *Nat. Nanotechnol.* **16**, 769–775 (2021).

[9] Mandal, S. *et al.* Destruction of superconductivity through phase fluctuations in ultrathin *a*-moge films. *Phys. Rev. B* **102**, 060501 (2020).

[10] Golod, T., Kapran, O. & Krasnov, V. Planar superconductor-ferromagnet-superconductor Josephson junctions as scanning-probe sensors. *Phys. Rev. Applied* **11**, 014062 (2019).

[11] Hovhannisyan, R. A., Golod, T. & Krasnov, V. M. Holographic reconstruction of magnetic field distribution in a Josephson junction from diffraction-like $I_c(H)$ patterns. *Phys. Rev. B* **105**, 214513 (2022).